Radiometer for the measurement of water vapor in the upper atmosphere from space

S. B. Calcutt, T. M. Pritchard, C. L. Hepplewhite, F. W. Taylor, S. T. Werrett, E. Arijs, and D. Nevejans

We describe the design, the development, and the calibration of a radiometer to measure water vapor abundance in the middle atmosphere, using the solar occultation technique from an orbiting platform. The use of gas cells containing water vapor and carbon dioxide leads to a relatively simple, but sensitive, design. This radiometer is shown to be capable of detecting water vapor in the mesosphere, where, because of dissociation by the Sun, the amounts are very small, of the order of 1 part per 10^6 or less. A flight version of the instrument will be launched in 1992 on board the European Retrievable Carrier space platform, and the data will be employed for a better understanding of the Earth's water budget.

Key words: Solar occultation, mesosphere, water vapor, calibration.

1. Introduction

Water vapor is important for the chemistry and the radiative balance of the atmosphere and is a crucial component of the terrestrial biosphere. In addition to its well-known roles in meteorology near the surface, it is the most important single contributor to the greenhouse effect, which determines surface temperatures globally, and therefore to the climate on our planet. Water vapor is highly variable in space and time and can be used as a tracer of atmospheric motions.

Measurements of water vapor in the upper atmosphere are limited, however, and its distribution and variability at high levels are not well known or understood.[1] Water is constantly being removed from the Earth near the upper boundary of the atmosphere because energetic solar radiation (wavelengths less than 242.6 nm) can dissociate H_2O to produce H and OH, the former being light enough to escape from the planet entirely. The actual rate at which this dissociation occurs is uncertain,[2] in part because of the difficulty of obtaining reliable measurements of water vapor amounts at the relevant altitudes, 50–100 km above the surface.

Water is also produced in the atmosphere, predominantly at rather lower levels in the middle atmosphere (10–50 km), by the photolysis of methane,[3] and the detailed balance among production, destruction, and vertical transport (from the troposphere) of middle atmosphere water vapor is one of the major longstanding questions in atmospheric physics. To complicate matters, this balance is, of course, globally and seasonally variable, and isolated measurements reveal much about local conditions but say little about the global distribution.

An instrument has been developed that will make new measurements of water vapor in the upper stratosphere and the mesosphere over an extended period of at least one year. With this we hope to shed light on the physical processes at work in the dissociation region. In this paper we describe the instrument concept and its design and implementation.

2. Previous Measurements and Experiment Rationale

Ground-based measurements of upper stratospheric and mesospheric water vapor are scarce, and the results are subject to considerable uncertainty.[4] It is impossible to say how much of this scatter, of up to 1 order of magnitude, is due to experimental error and how much is due to true atmospheric variability.

Observations from satellites offer the best potential solution to the problem of understanding the behavior of very variable atmospheric minor constituents. During the last two decades water vapor has been the target for a number of sophisticated sensors, of which the most important have been the LIMS[5] and SAMS[6] radiometers on Nimbus 7, which was launched in 1978, and the ATMOS spectrometer,[7] which was part

E. Arijs and D. Nevejans are with the Belgian Institute for Space Aeronomy, Brussels, Belgium. All the others are with the Department of Physics, Atmospheric Oceanic and Planetary Physics, Oxford University, Oxford OX1 3PU, UK.

Received 31 July 1992.
0003-6935/93/336764-13$06.00/0.

of the payload of Spacelab 3 in May 1985. Although making major progress, each was limited in some way. The first two were emission instruments, observing thermal emission from atmospheric water vapor at wavelengths near 6.3 μm and 20–100 μm, respectively, and tended to reach their limit of sensitivity below the dissociation region. For example, even though the highly sensitive pressure-modulated gas correlation technique was used in the SAMS instrument, its vertical coverage was limited to below 50 km. ATMOS, on the other hand, used the Sun as a source and observed water in absorption, which produced profiles up to approximately 80 km.[8] The extension in height range was made possible by the high sensitivity available when the Sun is used as a source. Another advantage of solar occultation measurements is low sensitivity to atmospheric temperature compared with that of emission measurements. Occultation measurements are, however, limited to observations made at local sunrise and sunset, which is not such a serious limitation for the investigation of water vapor as it is for studies of very short-lived species, such as some of the interesting nitrogen and chlorine compounds. The spatial coverage obtained with ATMOS was limited by the short duration of the flight (less than one week).

Our objective in developing a new instrument for measurement of water vapor was to extend the latitudinal coverage of water vapor measurements made over the altitude range 50–80 km. The solar occultation technique was adopted to permit the use of a very simple instrument and, in view of the variability of earlier measurements, to provide comparison with highly sensitive thermal emission instruments being developed over the same period. We chose to use the gas correlation technique because experience with instruments for the Nimbus satellite program[9] has shown that the multiplex advantage, whereby hundreds of spectral lines are observed simultaneously with high effective spectral resolution on each, can be combined with a simple and rugged instrument design. The following sections describe the development and the testing of such an instrument, known as the EURECA (European Retrievable Carrier) Occultation Radiometer (EOR). The EOR is part of a two-experiment package called the Occultation Radiometer. The second experiment, which measures aerosol extinction, was designed by the Belgian Institute for Space Aeronomy, who built the instrument structure and the data systems and also managed the interface with the European Space Agency for the whole instrument. The Occultation Radiometer is part of the payload of the EURECA space platform, which is launched by the shuttle and returned to Earth, again by the shuttle, approximately one year later.

3. Instrument Concept

A. General

Figure 1 shows the conceptual design of one of the two channels of the EOR. The two channels are

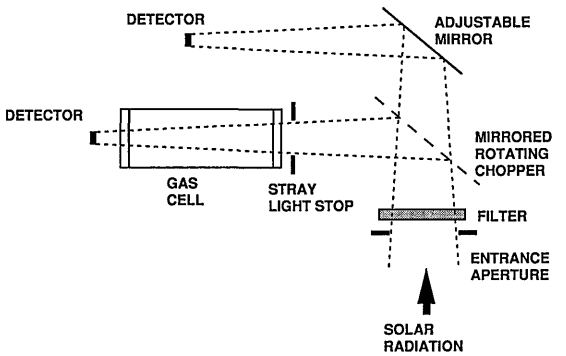

Fig. 1. Conceptual design of one of the two channels of the EOR.

identical except for the spectral response profile of the interference filter and the gas in the absorption cell. Each channel has two optical arms, one containing an absorption cell and the other not. The incoming beam, after passing through the filter, is switched between the two with a mirrored rotating chopper disk. No attempt is made to balance the two arms optically; instead, the electronic gain is set so that they both have approximately the same response to a given target. This very simple arrangement is possible because occultation radiometers are inherently self-calibrating. For most of each orbit both channels view the Sun without attenuation, while at the end of the atmospheric scan, which lasts approximately one minute per occultation, the source is completely obscured by the solid Earth. Thus full-scale and radiometric zero are sampled just before and just after every data acquisition pass.

In each channel the presence of a path of gas in one arm renders the signal in that arm insensitive to the presence of the same gas in the atmosphere, since the relevant wavelengths are already strongly absorbed. The arm without the cell, on the other hand, suffers a drop in signal because of attenuation by the atmospheric gas. Careful measurement of both signals permits the amount of gas in the atmosphere to be estimated, as described below. Simultaneous measurement of both CO_2 and H_2O permits the mixing ratio of the latter to be inferred, if it can be assumed that carbon dioxide is uniformly mixed. This is a common assumption, which is probably valid in the stratosphere, although caution is needed for higher levels. We return to this point below.

Figure 2 shows the differential absorption (difference in transmission between the cell and noncell arms) that was calculated for a model atmosphere[10] and the EOR H_2O and CO_2 passbands with a well-tested and proven line-by-line radiative transfer algorithm[11] and the Curtis–Godson approximation[12] to represent the inhomogeneous atmospheric path. Constant volume mixing ratios of 1 part in 10^6 for H_2O and 300 parts in 10^6 for CO_2 were assumed at all levels for this exercise. The lower cutoff in height coverage is unimportant provided that it is below 50 km, where thermal emission measurements will be available from other spacecraft instruments. It was arbitrarily taken to occur when the absorption reaches

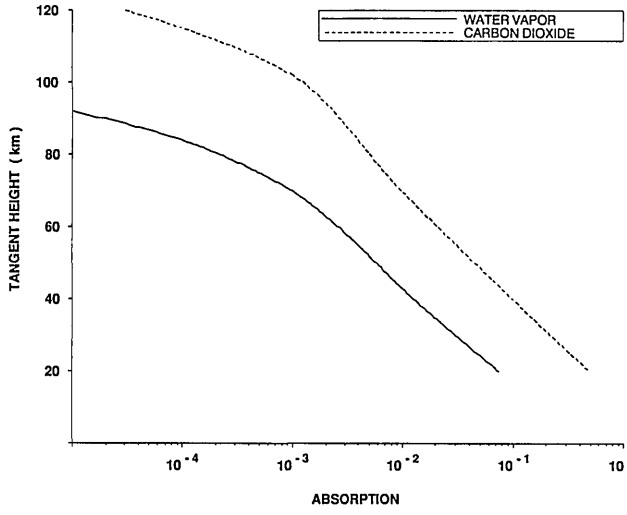

Fig. 2. Absorption due to water vapor and carbon dioxide in the EOR passbands calculated for a model atmosphere with $[H_2O] = 1$ part in 10^6 and $[CO_2] = 300$ parts in 10^6.

0.2. The upper cutoff occurs where the absorption falls below the minimum detectable value of $\leq 10^{-4}$ (Section 11 below). With these criteria the active measurement ranges for the EOR are from approximately 20 km to at least 85 km for H_2O and from approximately 30 km to at least 100 km for CO_2.

Since we chose to use the gas correlation technique in the solar occultation mode, the principal design parameters are the field of view, which affects the vertical resolution of the atmospheric measurements, the spectral bands to be employed, and the use of pressure modulation or conventional chopping. We consider each in turn below.

B. Field of View

The EURECA spacecraft was designed for microgravity research, which requires a very stable environment. This requirement excludes the articulation of large masses, such as solar panels, and any attempt to reorient the spacecraft continuously, which is necessary, for example, if it is to retain a constant orientation with regard to the surface of the Earth. Instead the platform faces the Sun continuously, and the solar panels are body fixed. This orientation is ideal for a Sun-viewing instrument like the EOR.

The angle subtended by the disk of the Sun is 0.54°, which, when it is viewed from the orbital height of EURECA (500 km), corresponds to a disk of approximately 25-km diameter at the tangent point in the atmospheric path. A more sophisticated experiment like ATMOS uses a sun tracker to select a portion of the center of the solar disk, approximately 2–4 km in projected extent at the limb, in order to obtain high spatial resolution in the atmosphere. However, Sun trackers are massive and complicated and would have placed the EOR experiment well beyond the available mass and volume resources allocated by the EURECA project. The pointing stability of the EURECA platform, at ±2°, is not good enough to guarantee that the instrument would see the Sun at all times if its field of view were small enough to resolve the solar disk. However, very high vertical resolution is not a requirement of the water vapor investigation described in Section 2, since we expect the water vapor profiles in the mesosphere to be smoothly varying with height. Even if they are not, the instrument as designed will smooth them, and this smoothing is not in conflict with our goal of measuring the water vapor amounts present at very high levels at all places and times and so of quantifying the destruction process. We therefore decided to make the EOR field of view large enough that the geometric resolution of the measurement would be determined by the size of the solar disk itself.

C. Pressure versus Altitude Measurements

The instrument will measure the absolute absorption, not the mixing ratio directly, of CO_2 and H_2O, versus the height as determined from the spacecraft ephemeris. The CO_2 channel, unlike the H_2O channel, is intended to measure pressure rather than mixing ratio, and the experiment design was based on the assumption that the mixing ratio could be taken to be constant up to the mesopause (85 km). In that case the water vapor mixing ratio as a function of height is readily determined from the measurements of both channels.

Pressure versus height determination by CO_2 observations is straightforward in the stratosphere, but there is now some evidence[13] that the CO_2 mixing ratio may fall off in the mesosphere much more dramatically than had been imagined when the EOR experiment was first designed. While there remains much uncertainty as to how reliable the measurements of depleted CO_2 are, and what causes the depletion, it is prudent to consider what the effect might be on the EOR investigation. In a single profile, without correlative measurements (of which there are none on EURECA, although some may be available from the NASA Upper Atmosphere Research Satellite, which will be in operation at the same time), it will not be possible to distinguish total pressure fluctuations from CO_2 depletion. Our strategy is to perform the retrievals initially in terms of the density (in units of inverse cubic meters) of both CO_2 and H_2O and then additionally to form profiles of water vapor mixing ratio on the assumption that CO_2 is well mixed up to the homopause (~ 100 km). Examination of the former profiles should reveal (from their shapes, from the correlation between CO_2 and H_2O fluctuations, and from latitudinal and seasonal variations) which fluctuations are due to pressure and which are due to mixing ratio variations. It should be possible, as a secondary scientific objective, to make a fresh statement about the stability of CO_2 in the mesosphere.

D. Spatial Coverage

The coverage of the Earth that will be obtained from a one-year mission can be calculated from the geometry

of the orbit. EURECA is to be placed in a 28.5°-inclination, 500-km-altitude circular orbit, which will precess in longitude by approximately 6.5° per day. The period provides 15 orbits (30 occultations) each day, each crossing the equator 24° further west than the previous one. The latitude of the observations varies only slowly throughout the mission as the solar longitude varies. The full latitude range of approximately +40° to −30° is covered in ~28 days by both the sunset and sunrise occultations. One occultation, defined as the time for the tangent height of the ray from the center of the Sun to the instrument to transit from 120- to 0-km altitude, or vice versa, lasts between 40 and 90 s depending on the orientation of the orbit with respect to the Sun.

E. Spectral Bands

The low mass and power available to the EOR precluded the use of cooled detectors, restricting the experiment to short wavelengths, where there is sufficient solar signal to make use of room-temperature detectors. The spectral limits of the two channels were chosen so that the H_2O and CO_2 channels were placed as close together in wavelength as possible, in order to make any effect that is due to scattering by particles similar for both. The n_3 band of H_2O and the $n_1 + n_3$ band of CO_2, centered at 3756 and 3716 cm^{-1}, respectively, overlap, but it is possible to select regions of strong absorption by each species without significant contamination from the other (Fig. 3). At these wavelengths the solar radiance is high enough that uncooled lead sulphide detectors can be used. Line-by-line transmission calculations were used to obtain synthetic spectra of the atmosphere at the levels of interest, and these calculations together with the above criteria, were used to select filters centered on 3900 cm^{-1} for H_2O and 3750 cm^{-1} for CO_2. In each case the full width at half-maximum is 70 cm^{-1} chosen as a compromise among overlap of species absorption, signal-to-noise ratio, and filter availability. Line-by-line calculations were used to determine that no other atmospheric gases contribute significantly to the absorption in these passbands.

F. Gas Correlation Technique

The Nimbus instruments, from which the EOR obtained much of its heritage, used two versions of the gas correlation technique. On Nimbus 4 and 5 selective chopping was used, in which the beam is passed alternately through full and empty cells and the difference signal is measured. Nimbus 6 and 7 used pressure modulation radiometry, in which the pressure of a single cell was modulated. The latter approach is intrinsically better balanced and is the preferred method for measurements for which the signal level is small and vulnerable to drifts in zero level and gain. However, the Nimbus instruments all measured thermal emission from the atmosphere and were not subject to the viewing-geometry constraints of Sun-viewing instruments. The latter

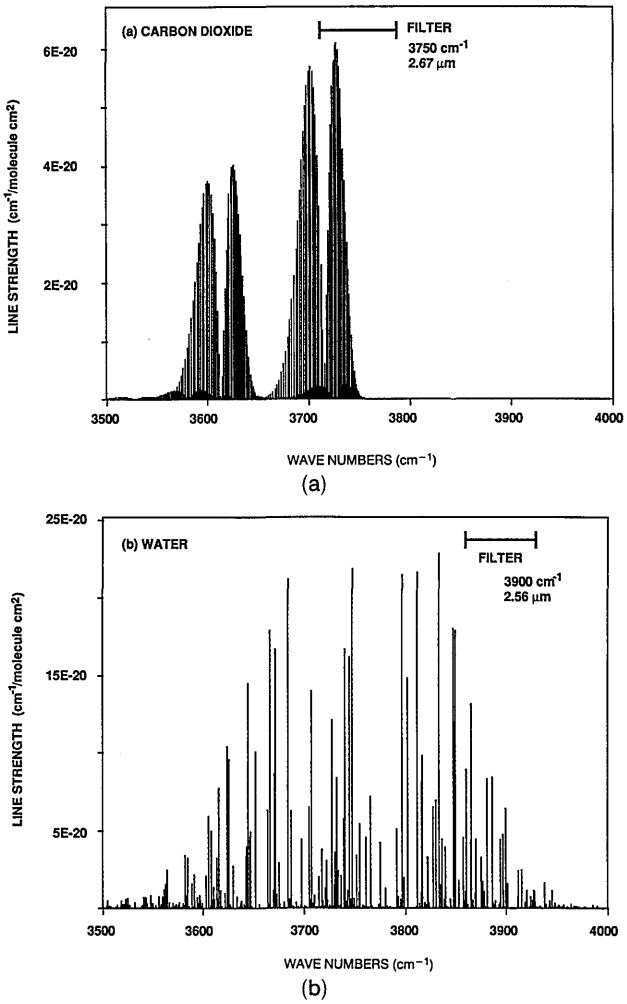

Fig. 3. Selection of spectral intervals for the H_2O and CO_2 channels showing the positions and the strengths of absorption lines for both gases.[14]

must deal with a large and variable Doppler shift of the atmospheric versus the instrumental spectral lines on account of the orbital velocity of the spacecraft and the rotation of the Earth. This Doppler shift mandates the use of a large cell pressure for broadening the lines to the point where correlation with the much narrower atmospheric lines can be guaranteed under all observing conditions. Pressure modulation is not efficient with these constraints, and the use of mechanical modulators also tends to exacerbate problems with the microgravity environment that the spacecraft is required to maintain. The traditional objection to selective chopping—the signal that is due to the gas can be masked by imbalance between the two optical paths as a result of other causes—is less valid for occultation measurements, in which calibrations are automatically obtained during the course of an occultation as the incoming intensity changes from full Sun to zero.

G. Absorption Cell Pressures

It is important to minimize the sensitivity of the instrument to these Doppler shifts over the full range

of such shifts. For the water vapor cell, where the maximum partial pressure is determined by the saturation vapor pressure, this minimization implies means maximizing the absorption at the peak Doppler shift with respect to the total pressure in the cell. This minimization was achieved by an increase in the pressure broadening through the addition of a quantity of nitrogen, which has no spectral lines of its own at these wavelengths. The optimum value for the total pressure can be estimated by differentiation with respect to pressure of the expression for the cell line shape at the peak Doppler shift to be encountered, which is 0.1 cm^{-1}. We confirmed this result using a line-by-line integration method to determine the depth and the shape of the atmospheric lines at various tangent heights and those of the cell at various pressures. Figures 4 and 5 show some results of these calculations for water vapor, which led to the choice of a filling pressure of 1 bar.

The large Doppler shift resulting from spacecraft orbital motion can be corrected from knowledge of the spacecraft orbit. Atmospheric winds, however, will introduce an unpredictable Doppler shift that will be minimized when the change in cell transmission is small over the range of shifts expected, i.e., at high total pressures. This effect was investigated by calculation of the ratio of the measured signal (defined as the difference between the absorptions measured in the arms with and without gas cells) to the combined errors introduced by digitization and atmospheric winds. This ratio increases with total cell pressure as the wing of the broad instrumental line crosses the narrow, Doppler-shifted atmospheric line and then levels out to a constant value once the atmospheric line is obscured by the core of the lines in the cell. At the same time the broad-band transmission of the cell falls, resulting in an undesirable loss of

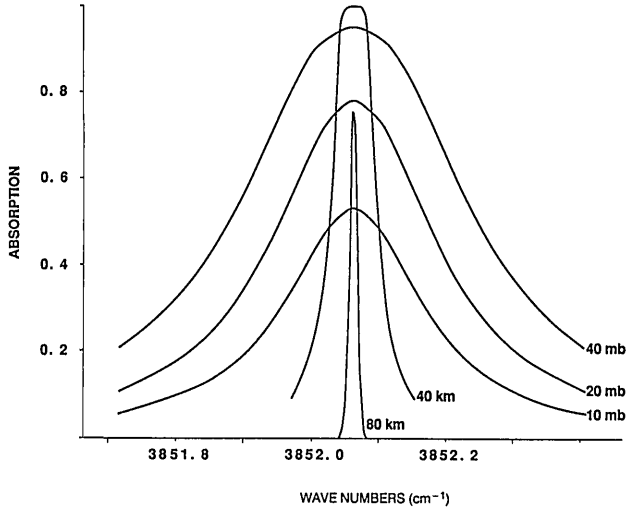

Fig. 4. Calculated profiles for the water vapor line at 3852.06 cm^{-1} (a typical strong line) under various conditions. The broad curves are for the cell at 303 K and a total pressure of 1 bar, with 10, 20, and 40 mbars of water vapor, respectively. The narrow curves are for the atmosphere at tangent heights of 40 and 80 km, respectively.

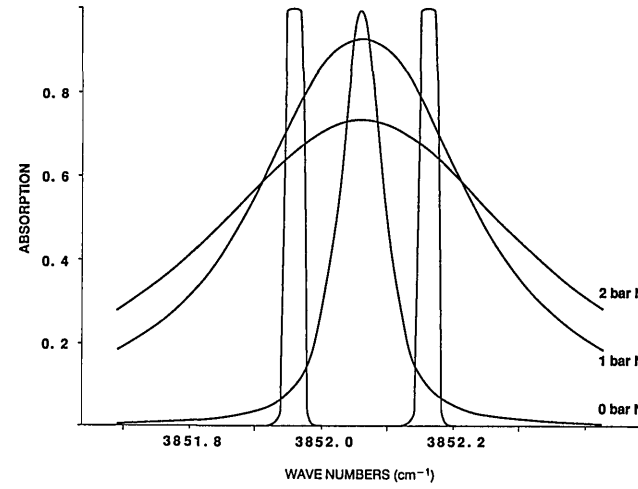

Fig. 5. Same as Fig. 4 but all the cell lines now have 35-mbar water vapor plus 0, 1, and 2 bars of nitrogen. The atmospheric line is calculated for 60 km and shown at the two extremes of Doppler shift to be encountered.

species selectivity. The total pressure of 1 bar, with 30 mbar of water vapor, determined as the optimum for yielding a uniform instrument response, was selected as a reasonable compromise among these effects. For the CO_2 cell the partial pressures of both gases could be varied without the constraint of condensation. Figure 6 shows the results of a similar study for CO_2, which led to 320 mbars of CO_2 in a total pressure of 700 mbars being selected as optimum.

4. Design of the Instrument

A. Layout

Figure 7 shows the layout of the instrument and the path taken by the incoming radiation to reach the four detectors. The following description is of one of the two channels; as already noted above, they are identical except for species and filter passband.

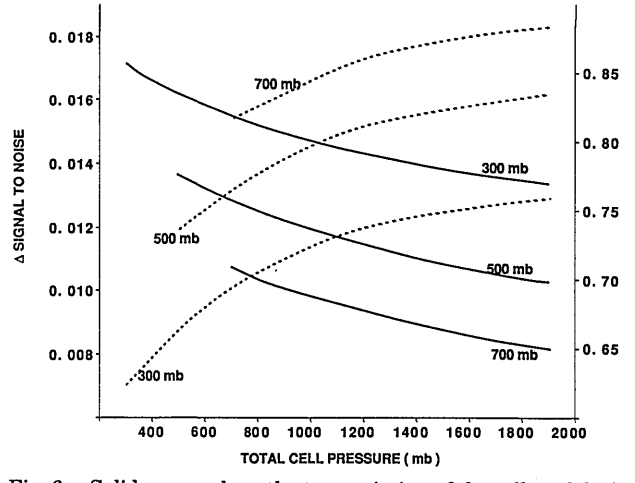

Fig. 6. Solid curves show the transmission of the cell, and dashed curves show the differential signal (i.e., cell minus no-cell paths) to noise ratio as a function of total cell pressure (CO_2 + N_2). The parameter on each curve is the CO_2 partial pressure in millibars.

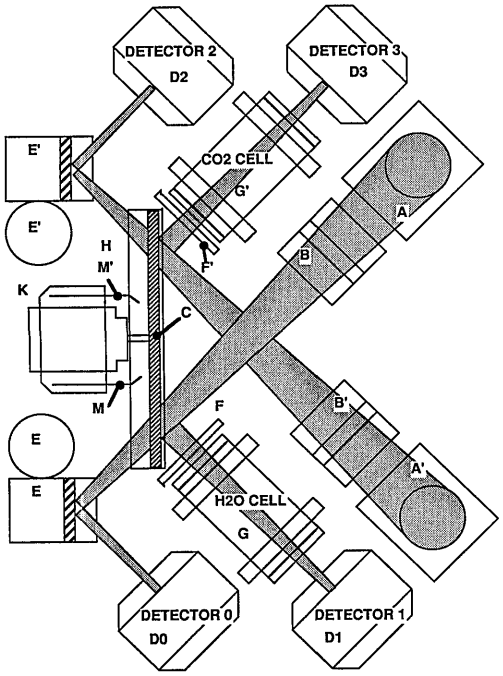

Fig. 7. EOR instrument layout.

Table 1 summarizes the nomenclature used for the four detectors. Solar radiation enters the instrument perpendicular to the diagram above the mirror (A). This mirror, with a polished aluminum surface inclined at 45° to the optical plane, deflects the beam into the plane of the diagram. The beam passes through an aperture stop attached to the filter mount (B) and the narrow-band interference filter, which selects the wavelength region of interest. The beam is then chopped by a four-blade rotating chopper (C), splitting the beam between the two arms as well as modulating it at a frequency of 533.3 Hz. One beam passes through the chopper and onto a detector (D0) after reflection by a plane mirror (E) adjustable in two dimensions, while the other, reflected off the chopper blade, passes through the gas cell (G) onto another detector (D1).

B. Gas Cells

The titanium gas cells are 50 mm long and of 19-mm internal diameter, with 3-mm-diameter copper filling pipes suitable for crimp sealing. The cell windows are sapphire, selected both for its transmission properties and to match the thermal expansion coefficient of titanium. Fiberglas mounts and an aluminized kapton blanket are used in conjunction with heaters and thermistors to thermostat both cells at a temperature near 30 °C.

Table 1. Identification of Detectors and Channels

Detector No.	Channel	Bandpass (cm^{-1})	Arm
0	Water vapor	3900 ± 35	No cell
1	Water vapor	3900 ± 35	Cell
2	Carbon dioxide	3750 ± 35	No cell
3	Carbon dioxide	3750 ± 35	Cell

C. Detectors

The detectors are 4 × 4 mm^2 lead sulphide photoconductors manufactured by Santa Barbara Research Center. The large size was chosen to maximize the signal-to-noise ratio, which, because of the absence of focusing optics, varies with the square root of detector area. Each detector was mounted with a preamplifier circuit board inside a separate housing on a thermostatted plate.

D. Optical Design

Various precautions were taken to suppress stray light. The whole optical path from the entrance aperture to the cells is enclosed in blackened baffles (not shown in Fig. 7). The envelope of rays that can reach the detectors directly is shown shaded. In addition, from each aperture there is an expanding conic envelope of additional rays that can enter the instrument. The stop (F) is sized so that this envelope does not reach the cell walls, thus preventing any reflected solar radiation from reaching the detector. The anodized motor mount (K) includes a background target (M) with a similar blackened surface to the rear of the chopper to ensure that each detector views a similar background when the chopper position is such that the incoming radiation is not directed onto that detector. The thermal radiation from within the instrument and from the Earth are well below the digitization limit even after accounting for the difference in field of view.

The spacecraft is expected to slew by up to 0.2° during a measurement. Had focusing optics been used, variations in the solar incidence angle might have led to changes in the attenuation by the optical components and movement of the image on the detector surface. To minimize this effect, the detectors have no foreoptics, and their angular field of view is determined simply by the angle, of approximately 0.5°, subtended by the solar disk. The entire detector surface is illuminated by the whole solar disk so that any effects that are due to detector inhomogeneity are also minimized. The spacecraft design ensures that the boresight of the EOR is always within 2° of the center of the Sun. The internal baffles were set, therefore, to admit rays subtending up to ±2.27°, so that the whole solar disk is always within the field of view.

E. Electronics

Figure 8 shows a schematic of the signal processing chain associated with one channel. Conventionally, the reference signal for the lock-in amplifier (phase-sensitive detector) is provided by an optical pickoff on the chopper followed by a circuit shifting the phase of the signal by an amount that is constant during measurements. Since for the EOR the source does not fill the field of view and can drift within it during an occultation, the relative phases of the solar signal

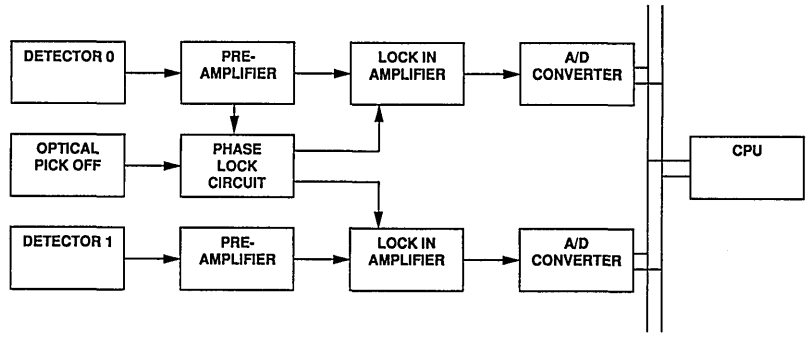

Fig. 8. Block diagram of EOR electronics.

and the optical reference can change by nearly 90°. A phase-lock circuit is therefore used to shift the pickoff signal into phase with one of the detector signals. This shifted reference is used for both arms so that the noise immunity of the difference signal is retained. When no solar signal is present, the reference is in phase with the optical pickoff signal, permitting a valid zero signal measurement.

F. Thermal Control

The largest thermal changes in the instrument and the spacecraft are likely to occur during solar occultation. Subsequent changes in the temperature of the detectors could lead to changes in their responsivity and hence in the signal output for constant irradiance. A particular threat is the thermal effect on the response caused by the changing amount of solar flux entering the instrument aperture, which would be very difficult to separate from the true radiometric signal if the former has a very short time constant. To overcome this possibility, we placed silicon windows in the entrance aperture to block wavelengths below 1 μm, which carry most of the solar radiant energy.

The two gas cells and the four detectors were thermally controlled with separate heaters and thermistors by means of a conventional three-term control algorithm, i.e., one in which heating rate is proportional to the weighted sum of the temperature difference from target temperature, the rate of change of temperature, and the time-integrated temperature difference. The thermostat accuracy is ±0.2 °C with continuous monitoring precision of ±0.02 °C. This limit was chosen to ensure that output changes that are due to temperature changes in the preamplifier gains are below the digitization limit.

In the EOR power budget there is sufficient power to heat only one heater fully at any given time, so the control software shares the heating on a priority basis. For example, if all six components are below their operating temperature by the same amount, all the heaters will be powered for the same amount of time with a switching frequency of 80 Hz. As the temperature approaches the operating value, the time that the heater is powered is reduced to favor points that are further from their target.

Initial values for the three gains of the temperature control loops were made based on measurements in vacuum of the heating rate of each item with full power on and of the subsequent cooling rate after power was removed. The weights were then iterated to minimize the time needed to reach stable conditions. These stabilization times were approximately 180 s for the detector assemblies and 1200 s for the gas cells, which are more massive than the detectors. The temperature stability was found to be approximately 0.02 °C (approximately the digitization limit for temperature measurements) over 100 s.

The change in sensitivity with respect to detector temperature was measured in vacuum by observation of the blackbody at a temperature of 775 K, which corresponds to an irradiance level equivalent to approximately 20% of full Sun. The measurements were made over a wide detector temperature range (25°–55 °C). Figure 9 shows the results for one detector. The sensitivities were found to be as great as 2.5%/°C. This sensitivity, combined with the temperature stability discussed above, implies a fractional drift in the signal of 5×10^{-4} during an occultation. The period of the measured drift was approximately 300 s, so that, during the short period of sounding the upper atmosphere (<20 s), a fractional drift of 10^{-4} can be expected. Based on the time constant of the detector assemblies, higher-

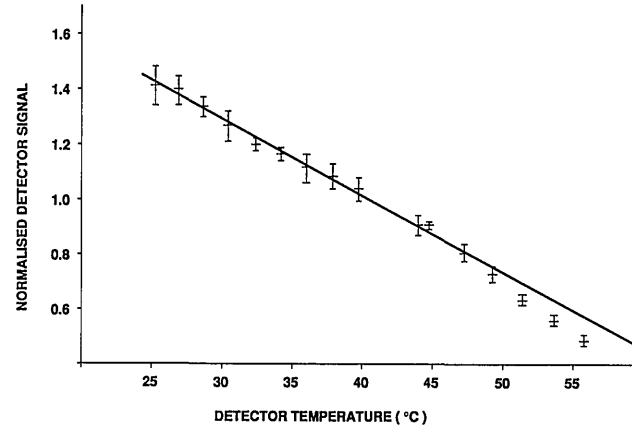

Fig. 9. Temperature dependence of detector sensitivity (channel 3).

frequency variations are not expected to appear above the digitization limit. If such variations occur, they would appear as noise in the measurements of stable sources (Section 11).

The thermal stability of the multilayer filters relies on the thermal control of the whole EOR subsystem. The maximum temperature variation, measured during thermal vaccum testing of the instrument, corresponds to a shift in the filters of ± 1 cm^{-1} and a change in signal of $< 0.5\%$.

5. Assembly

Assembly of the components onto a flat baseplate was a straightforward operation, with the exception of the filling of the gas cells. The cells were filled with high-purity gases, and the entire filling rig was thermostatted during the process. After filling was completed, the spectral transmission profiles of the cells were measured on a spectrometer and compared with computed spectra corresponding to the fill pressure. Good agreement was found with the computed spectra, indicating the absence of any spectroscopically active contaminants in the cell gas. The use of titanium as the cell material minimizes adsorption of water onto the cell walls, but as a precaution the entire process was repeated six times on 24-hour centers and checked for stability. Finally, the filling tube was crimped and sealed, and the cell contents were checked periodically thereafter with the spectrometer. No change in the cell transmission was measured, but, based on cell leak testing measurements, any change in the cell pressure should be $< 1\%$ of the initial value over 20 months. This value has been included in our current calculation of error limits, but the ultimate check on the stability of the cells against small leaks or chemisorption will be made after recovery of the instrument from orbit.

6. Calibration Objectives

Solar occultation measurements are inherently self-calibrating (Subsection 3.A). To make use of the results, however, one must still perform the following tasks:

(1) Verify that the instrument is insensitive to the expected drifts in the Sun pointing of the EURECA platform;

(2) Measure the noise level on the signals, which determines the maximum height sounded in the atmosphere;

(3) Verify that the assumption of a linear response of the detectors is valid and does not lead to errors larger than the instrument noise.

Most of these tasks can be performed in oribit between occultations (Section 12). The objective of the laboratory tests described here was thus to verify that the instrument will be able to make the atmospheric measurements planned rather than to produce a definitive calibration of the instrument.

7. Calibration Equipment

A. Vacuum Chamber and Control Systems

The measurements were carried out in a 0.5-m-diameter, 1.2-m-long vacuum chamber constructed for the purpose and containing a flat optical bench mounted on steel rails. For measurements of signals and noise the EOR was bolted to the optical bench facing an attenuator mounting wheel and an infrared source, all on adjustable mounts (Fig. 10). The control and data handling electronics, the power supplies, and the vacuum, thermal control, and command equipment were mounted external to the tank.

B. Solar Simulator

In order to set the radiometric gains correctly and to measure the linearity of response over the appropriate part of the dynamic range, we designed the source to provide approximately the same irradiation as the Sun in both of the spectral channels of the radiometer, at 2.56 and 2.67 μm. Since it is very difficult to manufacture an extended source with the effective temperature of the Sun (approximately 5850 K) in the laboratory, we increased the field of view to obtain the same approximate irradiance on the detectors as that expected when the radiometer views the Sun in orbit.

As described above, the field of view of the EOR is defined by the angular size of the Sun, approximately 0.5°. The acceptance angle range is defined to be 4.54° by baffles in the instrument; this angle is just sufficient to accept the whole solar disk under all pointing conditions after allowing for the pointing limitations of the attitude control system of the platform. Filling this maximum field with a blackbody at 1145 K produces the same irradiance at 3900 cm^{-1} at the detector as does the Sun viewed from Earth orbit. Figure 11 shows a schematic of a source designed to perform as a blackbody at temperatures up to approximately 1100 K. It consists of a Purox sheath with a commercial nichrome heating coil, mounted on outgassed graphite spacers inside a radiation shield and surrounded by a water-cooled jacket. A 44-mm-diameter, 100-mm-long cylindrical light pipe was mounted in the entrance to the sheath as shown to scramble the outgoing radiation and to

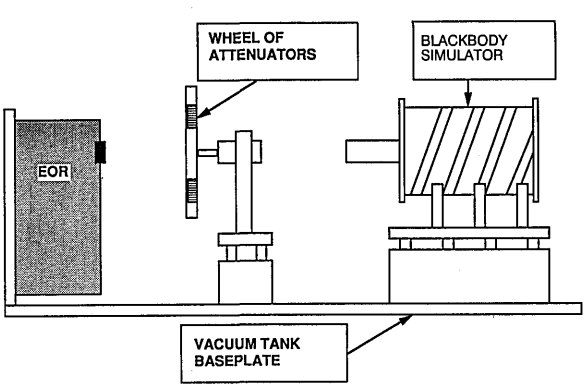

Fig. 10. Layout of units inside the test and calibration vacuum chamber, approximately to scale.

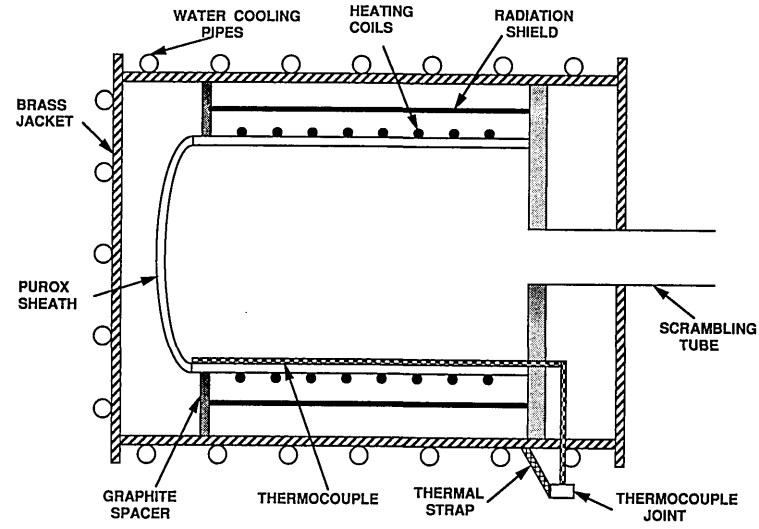

Fig. 11. Schematic diagram of the blackbody source used to simulate the Sun.

eliminate any residual inhomogeneities. The central 30 mm of the 44-mm aperture is used as the source.

C. Attenuator Wheel

One could vary the radiance entering the instrument from the maximum unattenuated value down to levels representative of those to be encountered during occultation by reducing the source temperature or by inserting any of three calibrated attenuators in the path between the source and the instrument. These were calcium fluoride neutral density filters with transmissions of 95% (2-mm CaF_2), 91% (4-mm CaF_2), and 61% (2-mm coated CaF_2). They were mounted on an attenuator wheel driven by a four-position stepper motor, with the fourth position open (i.e., 100% transmission).

D. Quartz Halogen Lamp

The blackbody was not suitable for all the measurements performed because of radiative heating of the instrument during long tests and because of its low temperature stability compared with the dynamic range of the instrument (2^{16}). For measurements for which high radiance and/or high stability but not radiometric accuracy were needed, a quartz halogen bulb mounted in an ellipsoidal reflector and powered from a battery was used.

8. Alignment and Field of View

The effects of small drifts in pointing, within the spacecraft budget of 2° overall, could be to alter the signal through small changes in the incidence angle onto the detectors. If this effect occurs during an occultation and is different in the two arms of one channel, the result would be indistinguishable from the atmospheric signal. If it is assumed that the signal at a detector varies with the cosine of the incidence angle (remembering that the instrument has no focusing optics), then an undetected misalignment of $dq°$ results in an error proportional to (sin 2°)dq if the maximum spacecraft tilt of 2° occurs during an occultation. The most stringent requirement would need this error to be less than the digitization error of 1 part in 2^{16}, which means dq must be less than $1.5 \times 10^{-5}/0.035$ rad, or approximately 0.01°.

In fact, the maximum rate of tilt of the spacecraft permitted by the microgravity constraint is 0.003° s^{-1}. In an occultation of 60-s duration the total tilt will not exceed 0.2°, which reduces the alignment requirement by 1 order of magnitude. Even so, to achieve better than 0.1° alignment accuracy required a two-stage postassembly alignment procedure, first using a laser with the filters removed and the detectors replaced with plane mirrors to centralize the beams and then using a collimated infrared source with the filters and detectors replaced for angular alignment. The final adjustment involved moving adjustable plane relay mirrors until a 2° slew of the incoming beam produced the same relative change in each arm of both channels. The primary aim was to ensure geometric alignment, but any optical differences in the two channels are compensated at the same time since the method relies directly on matching the radiometric response in the two arms. The balance measured during the alignment was 0.1% of full signal, which corresponds to the noise on these measurements and so represents an upper limit on the residual error. The sensitive upper atmosphere measurements within approximately 20 s of the full-Sun calibration can correspond only to a relative slew of up to 0.06°. Scaling the resulting error in radiance linearly from the error measured in the test facility for a 2° maximum slew, the maximum excursion permitted by the spacecraft specification gives an error in measured absorption of 3×10^{-5}, which is a factor of 3 smaller than the measured random error that is due to detector noise (Subsection 11).

The magnitude of the effect of spacecraft pointing drifts will be monitored periodically throughout the mission with measurements of the differential drifts

in the two arms of one channel during observation of the Sun away from occultation. This will also characterize any alignment changes during or after launch.

The change in beam angle caused by the maximum spacecraft slews of 2° does not cause a significant change in transmission or reflection of the optics. The slews do, however, slightly change the portion of the optics illuminated, so that differential contamination of the optical surfaces can cause signal changes indistinguishable from atmospheric absorptions. Once again the magnitude of this effect can be monitored in flight.

Irregularities in the field of view are of minor importance provided that they are similar in both arms of each channel, i.e., that they are due to imperfections in the shared optics. As a test for any gross alignment or throughput differences between the two arms in each channel, a near-collimated (0.5° divergence) beam was directed into the instrument and a 0.7-mm-wide slit was moved across the 25-mm-diameter entrance aperture. Figure 12(a) shows the output from each arm of the H_2O channel as the slit is scanned in the direction corresponding to the detector diagonal, and Fig. 12(b) shows the output for a scan across the full width of the detector. The width of the output functions corresponds to the divergence of the beam. The agreement between the two arms is within the measurement accuracy, itself limited by the accuracy of determining slit position, except at the edge of the scan in Fig. 12(b). This effect was found to be caused by reflection of the diverging beams from the cell walls in one of the arms and can be neglected for flight data anlaysis.

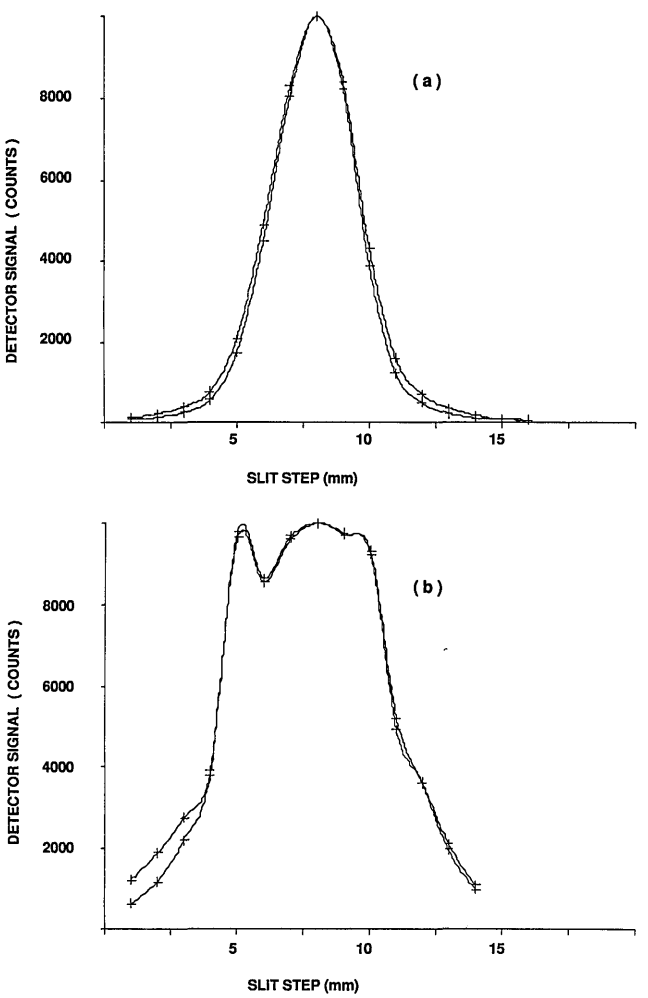

Fig. 12. Results of the field-of-view mapping test for the two water vapor channels: (a) diagonally scanned slit, (b) vertically scanned slit.

Figure 12(b) also shows a defect in the shared optics, leading to an ~10% dip in the response profile in both arms of the H_2O channel. This defect could affect the intensity versus height profiles, although again only if the spacecraft slews during an occultation. One can use the calibration scans to derive a limit on the additional error introduced into the retrievals by this effect but not to eliminate the problem, since there is no way to know whether rays reaching the detector have passed through this part of the optics, because the alignment status cannot be monitored during an occultation. Again, the slew rate restrictions on the spacecraft limit the magnitude of this effect to less than 1% of the radiance in each arm, since the optical axis can slew by no more than 10% of the angular size of the Sun between calibration and measurement. The relative response to the anomaly in the two arms is identical to within the accuracy of measurement; hence the effect on the profiles is expected to be negligible.

9. Radiometric Calibration

Absolute radiometric calibration is not required to high accuracy, as its only function is to check that the gain settings for the channels are correct. The signal channels, designed and supplied by collaborators at the Belgian Institute for Space Aeronomy, have switchable gains proportional to $10^{1.5n/20}$, with n varying from 0 to 15 to provide a large dynamic range.

To perform radiometric calibration, the EOR was mounted in the vacuum chamber with its entrance aperture fully illuminated by the blackbody. The detector outputs were measured as a function of blackbody radiance. Results for a typical detector are shown graphically in Fig. 13. The discontinuity in the response in this plot results from the jump in phase that occurs when the detector signal drops below the threshold of the phase-locking circuit (Subsection 4.E).

The errors in the blackbody radiance are large because of limitations in the ability to control the blackbody temperature. In practice, the blackbody was operated below its design temperature of 1100 K, so that the fluxes on the detectors corresponding to the maximum source radiances plotted are almost a factor of 2 below those expected for full-Sun views in orbit. This radiance level was adequate to demonstrate that the gains are set appropriately.

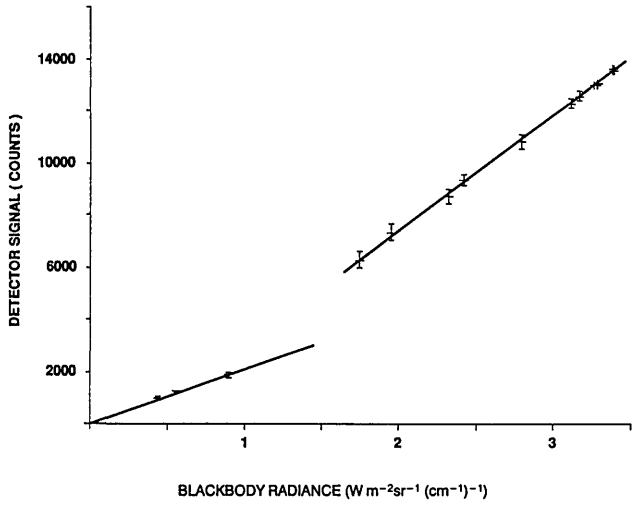

Fig. 13. Signal output from one of the four EOR detectors as a function of source radiance.

10. Linearity

For data analysis purposes the response of the instrument is assumed to be linear between the zero- and full-scale signals measured at the bottom and the top of the atmospheric profile, respectively. The measurements described in this section were designed to detect and to quantify any errors introduced by this assumption.

Linearity measurements are simple in principle. The output of each of the detectors is sampled at several known source radiances. The measurements were performed both with the blackbody source in vacuum and with a quartz halogen bulb in air. The latter was powered from a dc battery and so was more stable than the blackbody, and it also permitted the measurements to be extended to higher radiance values. The biggest problem encountered in this procedure is that of keeping the source radiance constant at an accurately known value during each measurement. These uncertainties limited the determination of the maximum error caused by nonlinearities in the instrument response function to 1% of the full-scale signal for each of the four detectors.

A more precise measurement of the maximum error introduced by nonlinearity as well as other sources was obtained with a filter wheel fitted with neutral density filters in front of the instrument aperture. For each value of source radiance the response in all four signal channels was measured for each of four filter wheel positions (100%, 96%, 91%, and 61% transmission). The transmittance and the spectral flatness of the neutral density filters over the passbands of the instrument was confirmed with a commercial grating spectrometer. The measured responses were used to calculate the quantity $DS_n(R_s)$, where

$$DS_n(R_s) = S_0(R_s) - S_n(R_s);$$

$S_0(R_s)$ is the signal with no filter, and $S_n(R_s)$ is the signal with the nth filter in place, both with source radiance R_s. $DS_n(R_s)$ was plotted against $S_0(R_s)$ for each of the filters. These plots should be lines of slope $1 - \tau_n$, where τ_n is the transmission of the nth filter. Departures from this line will be due to nonlinearity, system noise, and measurement error. The error in $DS_n(R_s)$ with respect to a fitted line will be the same magnitude as the expected error in determining the atmospheric transmission in flight, since $DS_n(R_s)$ is directly analogous to a measured absorption. This error can therefore be used directly as an estimate of the uncertainty in water vapor mixing ratio.

Figure 14 shows some typical results for one detector and one filter ($\tau_2 = 91\%$). The plots include linear fits to the data along with envelopes for 1% and 5% errors in measured absorption. Using all the available data, we deduced the following:

(1) The deviation from a linear fit is dominated by random and not systematic errors;
(2) The uncertainty ($3s$) in a single measurement of τ is typically 5% of its value or less.

Because of (1) and because of the known (Section 11) system noise for the instrument, (2) is probably due to measurement errors of the calibration procedure and therefore represents an upper limit on what will be obtained in flight. In the upper part of the range of vertical coverage, where the most scientifically valuable data are obtained ($z > 50$ km), the absorption due to water vapor is weak; i.e., the transmission of the atmospheric path is directly proportional to the mass of water present. There we expect to obtain the mixing ratio with a precision of 5% or better. This precision obviously will deteriorate at the highest and lowest levels as the transmission tends to unity and zero, respectively, and the signal becomes lost in the random system noise.

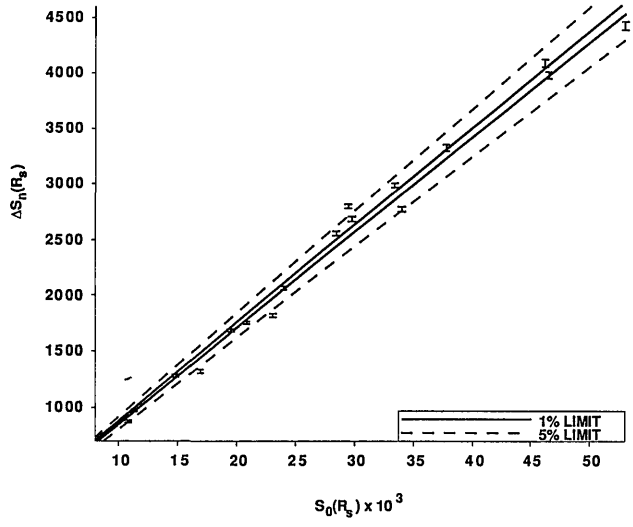

Fig. 14. Linearity measurements for one of the four signal chains for a neutral density filter with $t = 0.908$ to simulate the atmosphere (see the text for details).

11. Random Noise

The signal chain was designed so that noise would be dominated by the intrinsic noise of the detectors with a D^* of 9×10^{10} cm $(\mathrm{Hz})^{1/2}/\mathrm{W}$ at 200 Hz with a total noise smaller than the digitization. Noise measurements were taken continuously throughout the calibration and were found to have a typical 1s variation of ≤ 4 counts, corresponding to an error in absorption measurement of 6×10^{-5} (the instrument has 16-bit resolution).

This measured noise is approximately 1 order of magnitude above the design noise level. There are four probable candidate sources for the additional noise: (1) additional detector noise, (2) detector temperature variations unresolved by the temperature measurements, (3) microphonic noise caused, for example, by vibration of the rotating chopper near the chopping frequency, and (4) electromagnetic interference from the laboratory environment. The two last-named sources will be less significant once the instrument is in orbit. Unfortunately, the realities of the delivery and launch schedule for the instrument did not permit enough time to complete the unambiguous determination of the noise source. Instead, the higher figure was used to assume an upper limit in fractional error of order 10^{-4} in a single absorption measurement, and this higher error was used to evaluate the expected instrument performance. This performance remains adequate to meet our primary scientific goal of water vapor measurements of an accuracy of 10% or less up to the mesopause.

12. In-Flight Calibration

As noted above, in-flight calibration is accomplished automatically by the geometry of the occultation. In addition, the following can be checked during flight:

(1) The effects of drift in the spacecraft pointing.
(2) The temperature dependence of the detector responsivity from an analysis of the calibration data over the natural range of instrument temperatures.
(3) The state of the water in the cell, particularly after the instrument has been switched off and has been cold, which is when water will condense. One performs this check by monitoring the signal in the two arms as the cell warms up.

Finally, use will be made of the plan to retrieve the EURECA spacecraft from orbit to check cell pressures, alignment, and other calibration variables after one year of flight.

13. Vertical Coverage and Resolution

The effective vertical resolution obtained when estimating the volume mixing ratio of water is determined by the convolution of the geometric resolution with the weighting of the measurement to lower altitudes by the drop in pressure with height. Figure 15 shows a calculated weighting function, i.e.,

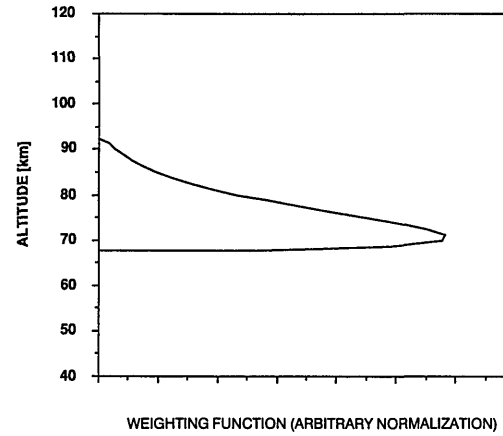

Fig. 15. Calculated weighting function for an EOR observation at a geometric tangent height of 85 km.

the sensitivity of a particular EOR measurement to changes in water mixing ratio at each altitude, corresponding to a geometric response centered on 85 km. The spread between half-power points is ~12 km, approximately half of the geometric field of view. Samples are taken every 0.2 s, in which time the mean tangent height changes by 0.2–0.6 km depending on the orientation of the spacecraft orbit with respect to the direction of the Sun. This oversampling in the vertical dimension by a factor of from 20 to 60 permits us to combine measurements in the profile retrieval process in a way that optimizes the trade-off between the uncertainty in the concentration values as a result of noise in the measurements and the vertical resolution finally obtained. This type of trade-off has been applied to atmospheric sounding by Conrath[15] using the methods of Backus and Gilbert.[16] Figure 16 shows a typical trade-off of noise versus vertical resolution, while Fig. 17 shows the error in determined mixing ratio versus altitude for several combinations of vertical resolution and sampling interval for the worst-case noise figures measured during testing (above).

The results show, for example, that at 80-km altitude a water vapor mixing ratio of 10^{-6} can be

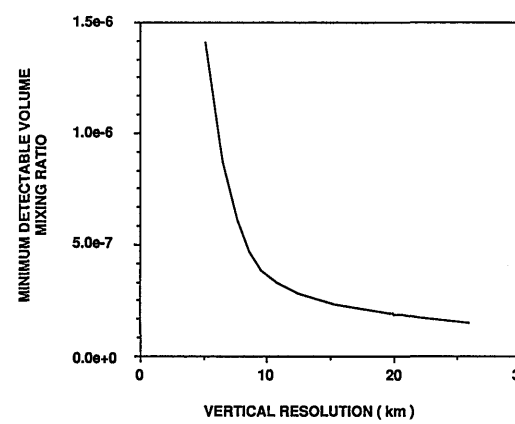

Fig. 16. Trade-off of noise versus vertical resolution for the EOR using the Backus–Gilbert algorithm for a tangent height of 80 km with 2-km sampling.

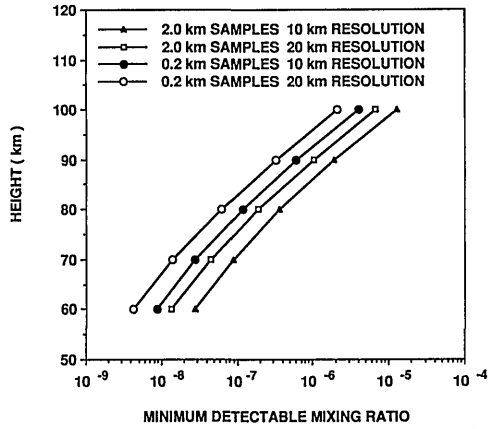

Fig. 17. Calculated error in mixing ratio versus altitude as a function of vertical resolution.

determined with an accuracy of 10% and a vertical resolution of 10 km. A similar vertical resolution with higher sensitivity is predicted for the CO_2 measurements.

The atmospheric absorption varies with atmospheric temperature by approximately 0.5%/K. This effect can, however, be largely removed by use of the measured pressure profile and the assumption of hydrostatic equilibrium.

The analysis does not include any errors in the tabulated line data used. Laboratory measurements of water vapor absorption in this spectral region for comparison with tabulated data have been made but have not yet been analyzed in detail.

14. Conclusion

We have described the design and the development of a simple space instrument that is to be used to answer some of the complex questions about the Earth's water vapor budget by measuring the humidity of the atmosphere at very high altitudes where water is being destroyed by photolysis. The instrument, as measured in the laboratory, is expected to be able to determine water vapor mixing ratios with an accuracy of 5%–10% or better up to altitudes of approximately 85 km. There may be additional sources of error that depend on factors such as spacecraft performance and instrument contamination, but their effects will not be known until flight data are available. The spacecraft was launched in July 1992, and the instrument appears to be functioning as expected.

We thank Rodney Knight of the Rutherford Appleton Laboratory for his assistance and expertise in filling the gas cells, G. Davis for his help in the development of the blackbody source, British Aerospace for its help in instrument mounting and vibration testing, and the UK Science and Engineering Research Council for financial assistance.

References

1. S. Solomon, E. E. Ferguson, D. W. Fahey, and P. J. Crutzen, "On the chemistry of H_2O, H_2, and meteoritic ions in the mesosphere and lower thermosphere," Planet. Space Sci. **30,** 1117–1126 (1982).
2. J. W. Chamberlain and D. M. Hunten, *Theory of Planetary Atmospheres* (Academic, New York, 1987), Chap. 3.
3. G. Brasseur and S. Solomon, *Aeronomy of the Middle Atmosphere* (Reidel, Dordrecht, The Netherlands, 1986), Chap. 5, p. 227.
4. T. M. Pritchard, "Studies of minor constituents in the atmosphere," Ph.D. dissertation (Department of Physics, Oxford University, Oxford, UK, 1988).
5. J. C. Gille and J. M. Russell, "The Limb Infrared Monitor of the Stratosphere: experiment description, performance and results," J. Geophys. Res. D **89,** 5125–5140 (1984).
6. F. W. Taylor, "Remote sounding of the middle atmosphere from satellites: the Stratospheric and Mesospheric Sounder experiment on Nimbus 7," Surv. Geophys. **9,** 123–148 (1987).
7. C. B. Farmer, "High resolution infrared spectroscopy of the Sun and the Earth's atmosphere from space," in *Proceedings of the 6th International Conference on Fourier Transform Spectroscopy,* G. Gruelachvili, R. Kellner, and G. Zerbi, eds., Mikrochim Acta (Wien) **3,** 189–214 (1987).
8. M. R. Gunson, C. B. Farmer, R. H. Norton, R. Zander, C. P. Rinsland, J. H. Shaw, and B.-C. Gao, "Measurement of CH_4, N_2O, CO, H_2O, and O_3 in the middle atmosphere by the Atmospheric Trace Molecule Spectroscopy experiment on Spacelab 3," J. Geophys. Res. D **95,** 13867–13882 (1990).
9. F. W. Taylor, "Nimbus meteorological satellites," in *Magill's Survey of Science: Space Exploration Series* (Salem, Pasadena, Calif., 1989), pp. 1072–1079.
10. *U.S. Standard Atmosphere* (1976 edition), NOAA-S/T 76-1562 (National Oceanographic and Atmospheric Administration, NASA, and U.S. Air Force, Washington, D.C., 1976).
11. D. P. Edwards, "GENLN2: the new Oxford line-by-line atmospheric transmittance/radiance model," internal publ. 87.2 (Department of Physics, Oxford University, Oxford, UK, 1987).
12. R. M. Goody and Y. L. Yung, *Atmospheric Radiation,* 2nd ed. (Oxford U. Press, New York, 1989), Chap. 6.
13. F. W. Taylor, "Studies of planetary atmospheres by optical methods," in *Progress in Atmospheric Physics* (Kluwer, Dordrecht, The Netherlands, 1988), pp. 33–46.
14. L. S. Rothman, R. R. Gamache, A. Goldman, L. R. Brown, R. A. Toth, H. M. Pickett, R. L. Poynter, J. M. Flaud, C. Camy-Peyret, A. Barbe, N. Husson, C. P. Rinsland, and M. A. H. Smith, "The HITRAN database: 1986 edition," Appl. Opt. **26,** 4058–4097 (1986).
15. B. J. Conrath, "Vertical resolution of temperature profiles obtained from remote radiation measurements," J. Atmos. Sci. **29,** 1262–1271 (1972).
16. G. E. Backus and J. E. Gilbert, "Uniqueness in the inversion of inaccurate gross earth data," Philos. Trans. R. Soc. London Ser. A **266,** 123–192 (1970).